

**Ultrafast phonon dynamics of epitaxial atomic layers of Bi on Si(111)**

Kunie Ishioka\* and Masahiro Kitajima†

*Nano Characterization Unit, National Institute for Materials Science, Tsukuba 305-0047, Japan*

Oleg V. Misochnik

*Institute of Solid State Physics, Russian Academy of Sciences, 142432 Chernogolovka, Moscow region, Russia*

Tadaaki Nagao

*International Center for Materials Nanoarchitectonics (WPI-MANA), National Institute for Materials Science, Tsukuba 305-0044, Japan and CREST, Japan Science and Technology Agency, 4-1-8 Honcho, Kawaguchi, Saitama, 332-0012, Japan*

(Received 22 November 2014; revised manuscript received 26 February 2015; published 25 March 2015)

Ultrathin bismuth (Bi) layers on Si(111)- $7 \times 7$  undergo a structural phase transformation with reducing the number of atomic layers at 3 bilayers (BL). We investigate the phonon dynamics of the Bi films close to the phase transformation by pump-probe reflectivity measurements. Coherent  $A_{1g}$  and  $E_g$  phonons at 3 and 2 THz are clearly observed for the Bi layers with thicknesses down to 3 BL, confirming their rhombohedral crystalline structure. The  $A_{1g}$  frequency exhibits an abrupt redshift and splits into two components at 3 BL, which are attributed to the vertical motions of Bi atoms localized at the surface and subsurface bilayers. The  $E_g$  frequency, by contrast, shows a gradual blueshift with reducing the thickness, possibly due to the lateral compressive stress at the Bi/Si interface. Below 3 BL, no coherent phonon signal is detected, in agreement with the phase transformation to the black-phosphoruslike structure. Our observations indicate that the vertical vibrations are significantly softened at 3 BL, but become almost as hard as those in the bulk crystal by adding another bilayer.

DOI: [10.1103/PhysRevB.91.125431](https://doi.org/10.1103/PhysRevB.91.125431)

PACS number(s): 78.47.J-, 63.20.kd, 81.05.Bx

**I. INTRODUCTION**

Bismuth (Bi) is a semimetal with a rhombohedral crystalline structure, formed by a stacking of (111)-oriented bilayers [Fig. 1(a)], in ambient conditions. Angle-resolved photoemission (ARPES) studies on clean Bi(111) surfaces [1,2] and ultrathin Bi films epitaxially grown on Si substrates [3,4] have revealed that the surface electronic states are highly metallic, with the quantum well states lying below the Fermi level, in contrast to the semimetallic bulk. Recently ultrathin Bi films attracted renewed attention because they were theoretically predicted to be a topological insulator [5–8]. Atomically thin layers of rhombohedral Bi are not readily realized, however. When grown epitaxially on a Si(111)- $7 \times 7$  surface, ultrathin Bi films undergo a phase transition with reducing the film thickness  $n$  from rhombohedral to a black-phosphoruslike structure, at 3 atomic bilayers (BL) [9]. This happens because the surface Bi atoms lose only one interbilayer bond in the black-phosphoruslike phase, whereas in the rhombohedral phase they lose all three bonds. As a result, the cohesive energy of the black-phosphoruslike phase becomes lower than the rhombohedral phase for  $n < 3$  BL. The electronic structure of the black-phosphoruslike films was reported to be less metallic, due to their covalently bonded paired layers, than the metallic surface states of the rhombohedral films [10]. The detailed atomic structures of the ultrathin films remain unexplored so far, though it is plausible, by analogy with the Bi(111) surface [11–13], that the topmost interbilayer spacing may expand with respect to the bulk.

Precise knowledge of phonon dynamics at surfaces is crucial not only to gain insight on the atomic structure but to understand the surface electronic properties, because the phonons can play important roles in carrier transport and superconductivity. However, information on the Bi surface phonons, whether on clean Bi(111) surface or on ultrathin films on Si, had been long obtained indirectly, e.g., from the linewidth in the ARPES measurements [14]. Recently, time-resolved ARPES studies [15,16] revealed periodic modulations in the binding energies of the surface state as well as the bulk Bi band at the frequency of the  $A_{1g}$  optical phonon, and thus visualized the surface phonon of Bi(111) directly in the time domain. The modulation amplitude for the surface state was too small for quantitative discussion, however. Inelastic helium atom scattering measurements also successfully observed surface and subsurface phonons of Bi(111) [13,17]. The experimentally obtained phonon-dispersion relation clearly exhibited a few low-frequency phonon modes, which were attributed to the acoustic phonons from the first and second topmost bilayers. High-frequency optical phonon modes were not so well resolved in these experiments. On the other hand, theoretical studies on the two-dimensional Bi(111) films predicted hardening of the  $A_{1g}$  and  $E_g$  optical phonons at the  $\Gamma$  point, and softening over the rest of the Brillouin zone, with decreasing thickness [18,19]. Their conclusion was contrary to the experimentally observed softening of the  $A_{1g}$  and  $E_g$  phonons with reducing the size of the Bi nanocrystals [20] and with reducing the thickness of the rhombohedral  $\text{Bi}_2\text{Se}_3$  nanoplatelets [21]. Thus, the surface phonons of Bi(111) leave controversy and deserve thorough experimental investigation.

The rhombohedral crystal structure of Bi is derived by elongating a simple cubic along the body diagonal. The Jones-Peierls distortion [22] makes the atomic positions along the body diagonal (trigonal axis) sensitive to the electronic

\*ishioka.kunie@nims.go.jp

†Present address: LxRay Co., Ltd. Nishinomiya, 663-8113 Japan.

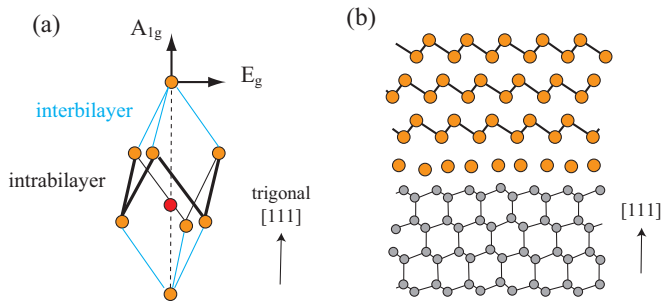


FIG. 1. (Color online) (a) Structure of rhombohedral Bi. Blue and black lines represent interbilayer and intrabilayer bonds. In the  $A_{1g}$  and  $E_g$  phonon modes the atoms move parallel and perpendicular to the trigonal (or [111]) axis [32]. (b) Schematic illustration of the 3-BL thick rhombohedral Bi on Si(111). Bi and Si atoms are colored yellow and gray.

distribution. This leads to the surprisingly efficient excitation of coherent  $A_{1g}$  phonons upon illumination of femtosecond optical pulses [23–25]. In the present study we examine the surface and subsurface phonon dynamics of ultrathin Bi layers epitaxially grown on Si(111). We observe the coherent  $A_{1g}$  and  $E_g$  phonons for the film thickness down to 3 BL, which is the critical thickness for the phase transformation. With reducing the film thickness, the  $A_{1g}$  frequency exhibits a sudden redshift and splitting at 3 BL, indicating the considerable softening of the interbilayer vibrations localized at the topmost and inner bilayers. By contrast, the  $E_g$  frequency shows a gradual blueshift with reducing the film thickness, possibly attributed to the Bi/Si lattice mismatch.

## II. EXPERIMENT

The samples studied are Bi films with different thicknesses  $n$  grown epitaxially on Si(111) substrates. Details of the sample preparation were described elsewhere [9,26]. In short, Bi is evaporated onto a clean Si(111)- $7 \times 7$  surface at room temperature in an ultrahigh vacuum chamber at a deposition rate of 0.43 ML/min. We define 1 monolayer (ML) as the density of Bi atoms in a pseudocubic Bi{110} plane, and 2 ML counts as 1 BL whose thickness is 3.9 Å. The crystalline structure of the Bi films is characterized *in situ* using low energy electron diffraction (LEED). We confirm that the Bi films of  $n \geq 3$  BL have the bulklike rhombohedral structure, as schematically shown in Fig. 1(b), whereas films of  $n < 3$  BL have the black-phosphoruslike structure [9]. For comparison, a 2-mm thick bulk single crystal Bi with a (111)-oriented surface and a clean Si wafer is also measured.

The samples are mounted in a closed-cycle cryostat and kept at 12 K. Pump-probe reflectivity measurements are performed in a near-back-reflection configuration using laser pulses with 800-nm center wavelength, 60-fs duration, and 76-MHz repetition rate. The 800-nm light can excite carriers along the  $\Gamma$ - $K$  line of Bi [27]. The penetration depth of the 800-nm light ( $1/\alpha = 14.7$  nm) is larger than the thickness of the films investigated (maximum 10 nm). Pump-induced changes in the total reflectivity  $\Delta R$  and in the anisotropic reflectivity  $\Delta R_{eo} = \Delta R_H - \Delta R_V$  are measured as a function of time delay between pump and probe pulses. For the  $\Delta R$

measurements, the pump and probe beams are vertically (V) and horizontally (H) polarized, respectively, with respect to the optical plane. For the  $\Delta R_{eo}$  measurements, the probe beam is polarized 45° with respect to the vertical, and the difference between the H- and V-polarized components of the reflected probe beam is recorded (EO sampling). The delay between the pump and probe pulses is varied either step-by-step with a conventional translation stage or repetitively at a 20 Hz rate [28]. The slow scan combined with the lock-in detection can detect both the nonoscillatory and oscillatory reflectivity changes undistorted, whereas the fast scan enables us to average the reflectivity signals over several thousand scans in a digital oscilloscope and thereby leads to high sensitivity specifically to the oscillations. In the fast scan measurements we remove the high- and low-frequency noises in the reflectivity signals by using a bandpass filter, typically set to pass 1–100 kHz, during the signal amplification. The frequency range for the bandpass filter is optimized so that it does not affect the oscillatory part of the reflectivity signal (several kHz) but cut off as much of everything else as possible. As a result, the nonoscillatory part of the reflectivity signals ( $\lesssim 100$  Hz), which cannot be clearly separated from the low-frequency noises, is also cut off.

## III. RESULTS

Figure 2(a) compares the reflectivity changes  $\Delta R/R$  of ultrathin Bi layers of different thicknesses, together with bulk Bi and Si, obtained from the slow scan measurements. The reflectivity traces for  $n \geq 3$  BL consist of the nonoscillatory and oscillatory components arising from the photoexcited carriers and coherent phonons, whereas no periodic oscillation is visible in the reflectivity for  $n < 3$  BL. The nonoscillatory component, which is fitted directly to the sum of two exponentially decaying functions indicated with broken curves in Fig. 2(a), rises and decays in 0.2 and 13 ps for bulk Bi. The time scales roughly correspond to the relaxation of heavy holes to the  $T$  point and their recombination with electrons [27,29]. For the 24- and 4-BL thick Bi films on Si, the decay time becomes significantly shorter (1.7 and 1.5 ps); the faster decay can be explained in terms of additional decay channels such as the metallic surface states [3,30,31] and scattering by defects. At  $n = 3$  BL,  $\Delta R/R$  first drops to a negative value with a time constant of 1 ps, and recovers in a time scale of  $> 100$  ps. The slow recovery from the negative value is characteristic to Si, as also shown in Fig. 2(a), and therefore attributed to the carrier dynamics in the substrate. However, the initial drop in the reflectivity is much slower than that of Si, indicating that it is contributed by the carrier relaxation within the Bi overlayer.

The oscillatory parts of the reflectivity changes consist of the  $A_{1g}$  and  $E_g$  modes at 3.06 and 2.14 THz for the bulk Bi, which are clearly visible as sharp Lorentzian peaks in the Fourier-transformed (FT) spectrum in Fig. 2(b). For the ultrathin Bi films, however, the  $E_g$  peak is small already at  $n = 24$  BL, and barely visible at  $n = 3$  BL, as shown in the same figure. To improve the signal-to-noise (S/N) ratio we perform the pump-probe reflectivity measurements using fast scan technique. Figure 3 compares the oscillatory parts of the total and anisotropic reflectivity changes  $\Delta R/R$  and  $\Delta R_{eo}/R$

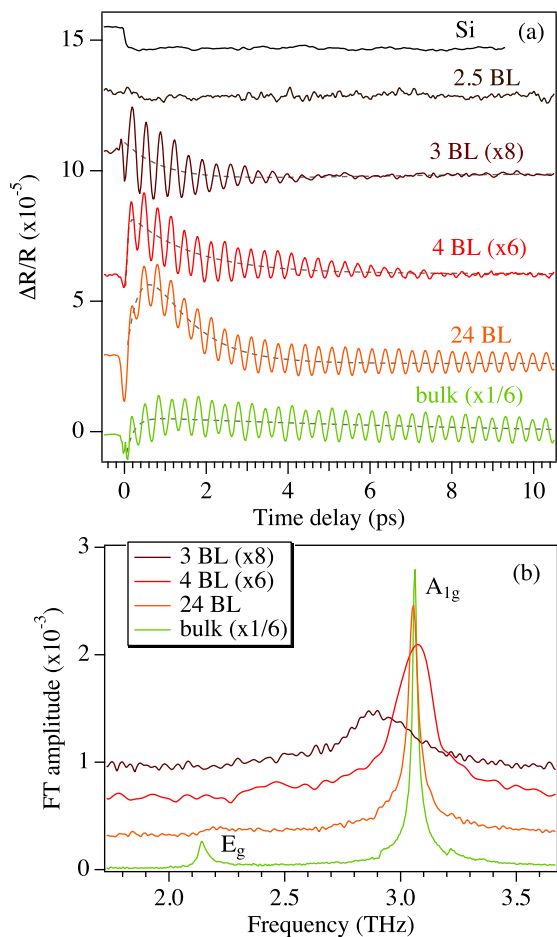


FIG. 2. (Color online) (a) Reflectivity changes  $\Delta R/R$  of the Bi layers with different thicknesses on Si(111) measured with slow scan and (b) the Fourier-transformed (FT) spectra of their oscillatory parts. Data from bulk single crystal Bi(111) and Si are also shown for comparison. Broken curves in (a) represent the nonoscillatory components. Traces are offset for clarity.

for  $n = 4$  and 3 BL; the nonoscillatory parts are removed by using a bandpass filter during the signal amplification.  $\Delta R/R$  is dominated by the  $A_{1g}$  mode, whereas the  $\Delta R_{eo}/R$  cancels the contribution of the totally symmetric  $A_{1g}$  mode and thereby emphasizes the  $E_g$  mode. In both cases, oscillatory parts of the time-domain signals are fitted directly to the sum of damped harmonic functions, each represented with [24]

$$f(t) = A \exp(-\Gamma t) \sin(2\pi \Omega t + \phi). \quad (1)$$

For  $n \geq 4$  BL, the sum of two damped harmonic functions, each representing the  $A_{1g}$  and  $E_g$  mode, is employed as the fitting function; for  $n = 3$  BL the fitting function is the sum of three damped harmonic functions, two of them corresponding to the frequency-split components of the  $A_{1g}$  mode and one to the  $E_g$  mode. First, we obtain the initial amplitudes  $A$ , the dephasing rates  $\Gamma$ , and the frequencies  $\Omega$  of the  $A_{1g}$  and  $E_g$  modes by fitting the  $\Delta R_{eo}/R$  signals directly to the fitting function. The  $E_g$  frequency and dephasing rate thus obtained are fixed during the fitting of the  $\Delta R/R$  oscillations to determine the  $A$ ,  $\Gamma$ , and  $\Omega$  of the  $A_{1g}$  mode precisely.

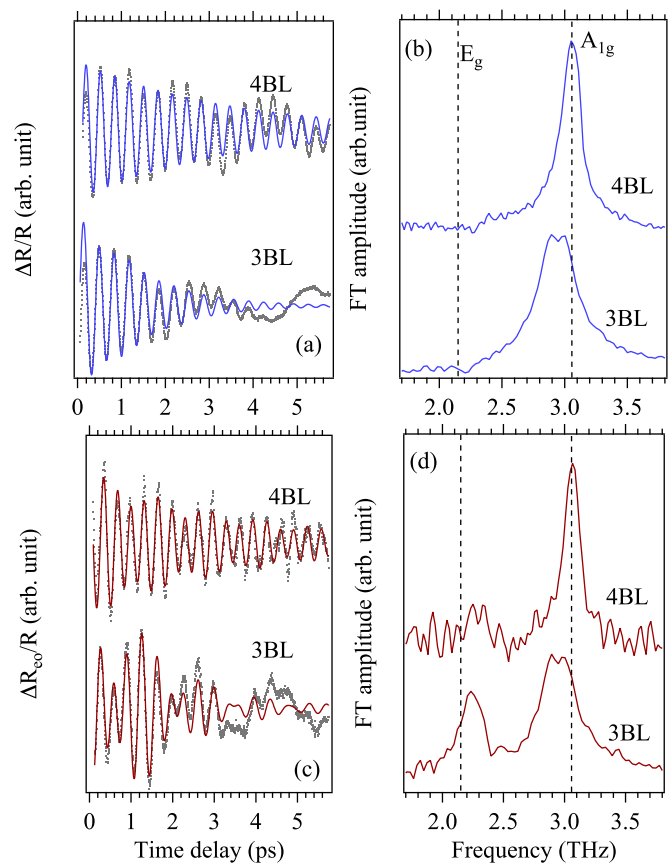


FIG. 3. (Color online) (a) and (c) Oscillatory parts of the reflectivity changes and (b) and (d) their FT spectra for 4- and 3-BL thick Bi layers measured with fast scan: (a) and (b)  $\Delta R/R$  and (c) and (d)  $\Delta R_{eo}/R$ . Dots and solid curves in (a) and (c) represent the experimental data and fits to the multiple damped harmonic functions. Broken lines in (b) and (d) represent the  $A_{1g}$  and  $E_g$  phonon frequencies for bulk Bi crystal. Traces are offset for clarity.

Figure 4 summarizes  $A$ ,  $\Gamma$ , and  $\Omega$  of the two optical phonon modes obtained from the time-domain fittings. We immediately notice the frequencies of the  $A_{1g}$  and  $E_g$  modes behave very differently as a function of film thickness  $n$ . The  $A_{1g}$  frequency is nearly independent of  $n$  for  $n \geq 4$  BL but exhibits a sudden redshift and splitting at  $n = 3$  BL, as is also obvious in the FT spectra in Fig. 3. The  $E_g$  frequency, by contrast, keeps blueshifting gradually with decreasing  $n$ . No frequency splitting is clearly observed for the  $E_g$  mode, partly because of its extremely small amplitude. In fact, the relative amplitude of the  $E_g$  mode to the  $A_{1g}$  mode for  $n = 4$  and 3 BL is an order of magnitude smaller than  $n = 24$  BL and the bulk, as shown in Fig. 4(c), making further quantitative analysis difficult.

To investigate the origin of the frequency splitting of the  $A_{1g}$  mode at  $n = 3$  BL, we examine the dependence of the coherent phonons on the pump density and pump polarization angle. The double-peaked line shape of the  $A_{1g}$  mode hardly changes with pump density, as shown in Fig. 5, indicating that the  $A_{1g}$  frequency splitting is not induced by photoexcited carriers but is an intrinsic nature of the 3-BL thick film. When we rotate the pump polarization angle  $\theta$  in the  $\Delta R/R$

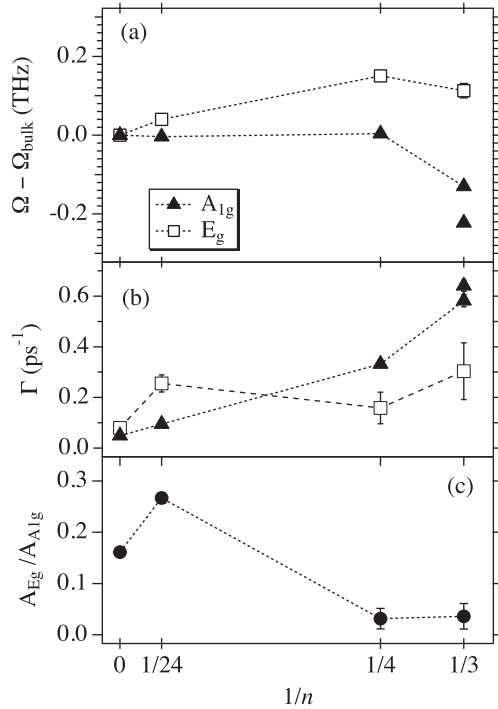


FIG. 4. Frequency shifts of the coherent phonons with respect to those of bulk Bi (a), their dephasing rates (b), and the relative amplitude of the  $E_g$  to  $A_{1g}$  phonons (c), as a function of inverse number of Bi bilayers on Si(111). Filled and open symbols in (a) and (b) represent the  $A_{1g}$  and  $E_g$  modes. Two symbols for the  $A_{1g}$  mode at  $n = 3$  BL in (a) and (b) represent the frequency-split components, whereas the  $A_{1g}$  amplitude at  $n = 3$  BL in (c) is estimated by assuming a single component. Inverse number of layers of 0 denotes the bulk single crystal Bi. The quantities are obtained by fitting the fast-scan reflectivity signals directly in the time domain, and the error bars represent the standard deviation of the fit coefficients. See text for details of the fitting.

measurements, the line shape of the  $A_{1g}$  mode appears hardly affected, as shown in Figs. 6(a) and 6(b). This is as expected for the  $A_{1g}$  mode detected in the back-scattering from the (111)-oriented Bi, since it has a Raman tensor (in rhombohedral

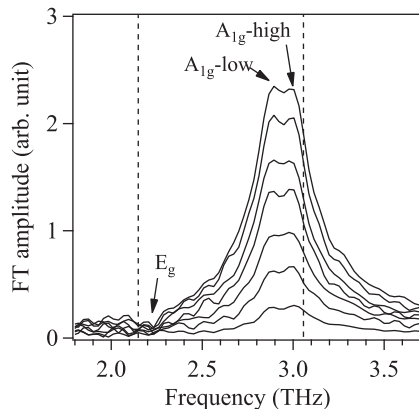


FIG. 5. FT spectra of the oscillatory parts of  $\Delta R/R$  of 3-BL Bi film measured at different pump densities from 6 to 43  $\mu\text{J}/\text{cm}^2$ .  $A_{1g}$  high and  $A_{1g}$  low denote two frequency-split components of the  $A_{1g}$  mode. Broken lines represent the  $A_{1g}$  and  $E_g$  frequencies for bulk Bi.

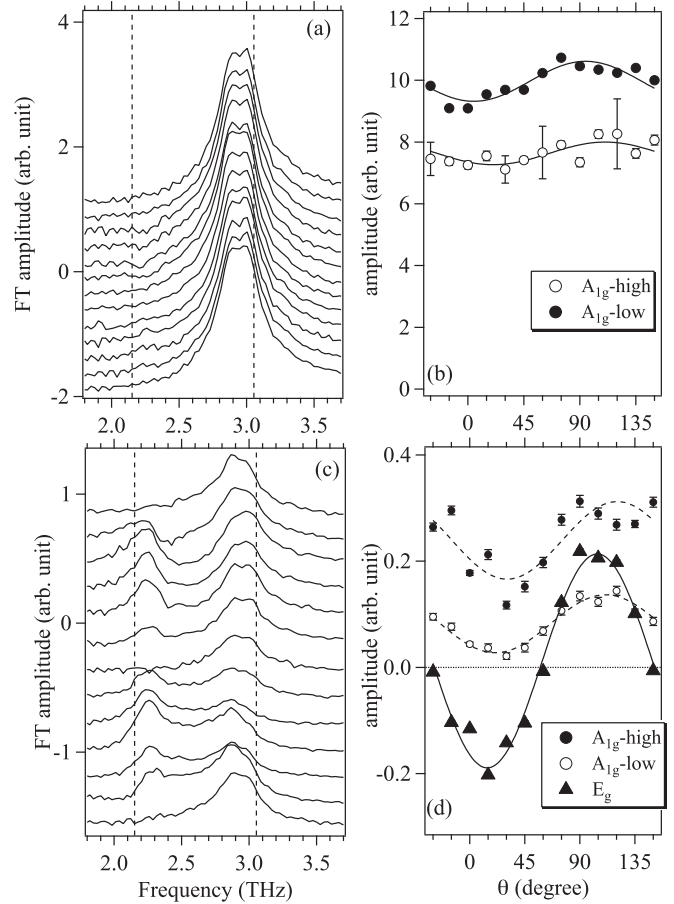


FIG. 6. (a) and (c) FT spectra of the oscillatory parts of  $\Delta R/R$  (a) and  $\Delta R_{eo}/R$  (c) of 3-BL Bi film measured at different pump polarization angles  $\theta$  between  $-30^\circ$  and  $150^\circ$  with respect to the optical plane. Traces are offset for clarity. (b) and (d) Amplitudes of the  $E_g$  mode and the frequency-split components of the  $A_{1g}$  mode as a function of  $\theta$ . The amplitudes are obtained by fitting the fast-scan reflectivity signals directly in the time domain, and the error bars represent the standard deviation of the fit coefficients. Curves are fit to  $B + C \cos 2\theta$ .

notation) [24,32],

$$\vec{R}_{A_{1g}} = \begin{pmatrix} a & 0 & 0 \\ 0 & a & 0 \\ 0 & 0 & b \end{pmatrix}. \quad (2)$$

However, in the  $\Delta R_{eo}/R$  measurements, in which the  $A_{1g}$  mode should be canceled [24], we find the  $A_{1g}$  mode amplitude larger than the  $E_g$  mode and exhibit a clear anisotropy, as shown in Figs. 6(c) and 6(d). The observed anisotropy suggests the contribution of the  $zz$  component as a result of a slight lattice misorientation. By contrast, the amplitude of the  $E_g$  mode appears to be proportional to  $\cos 2\theta$  [Figs. 6(c) and 6(d)], as expected from its Raman tensor (in the rhombohedral notation):

$$\vec{R}_{E_g} = \begin{pmatrix} c & 0 & 0 \\ 0 & -c & d \\ 0 & d & 0 \end{pmatrix}, \begin{pmatrix} 0 & c & -d \\ c & 0 & 0 \\ -d & 0 & 0 \end{pmatrix}, \quad (3)$$

though there may be a small deviation, comparable with the scatter of the data points, due to the misorientation.

#### IV. DISCUSSION

In the previous time-resolved ARPES studies on the Bi(111) surface [15,16], periodic modulations in the binding energies at the  $A_{1g}$  frequency were reported both for the surface state and the bulk Bi band. Though this observation gave a direct evidence for the coupling of both the electronic states to the  $A_{1g}$  mode, the frequency for the surface state was not given because of the extremely small modulation amplitude. In a time-resolved ARPES study on the rhombohedral  $\text{Bi}_2\text{Se}_3$ , however, similar modulations were observed more clearly for both the bulk band and the surface state [33]. Indeed, the modulation for the surface state had two frequencies, 2.05 and 2.23 THz, in contrast with a single frequency for the bulk band, 2.23 THz. The lower-frequency mode for the surface state was attributed to the topmost layer whose vertical motions are softened due to the reduction of the restorative van der Waals force at the surface, whereas the higher frequency was attributed to the bulklike inner layers [33].

For the ultrathin films grown on Si(111), the lattice parameters have not been reported so far. On the clean Bi(111) surface, on the other hand, the LEED study [11] and helium atom scattering [12,13] studies reported the slight expansion for the first *interbilayer* spacing with respect to the bulk, while the first *intra*bilayer spacing showed no significant relaxation. DFPT calculations without spin-orbit coupling also supported the expansion of the topmost bilayer spacing [13]. We therefore consider the vertical motions are also softened at the top bilayers of Bi on Si(111), and attribute the frequency-split components of the  $A_{1g}$  mode at the lower and higher frequencies to the topmost and inner bilayers of the 3-BL thick film. This assignment is consistent with the  $\theta$  dependence of the two  $A_{1g}$  components (Fig. 6), since the topmost and inner bilayers should share the same symmetry within the lateral plane, even if it is misoriented. The softened interbilayer structure is stabilized substantially by adding another bilayer, as is indicated by the almost bulklike frequency at  $n = 4$  BL. This stabilization corresponds to the steep decrease in the cohesive energy with increasing thickness [9].

Unlike the  $A_{1g}$  mode, the  $E_g$  frequency shows a blueshift with respect to the bulk Bi already at  $n = 24$  BL, and the blueshift increases gradually with decreasing film thickness. We attribute the observed blueshift to the compressive stress arising from the small but finite lattice mismatch between Bi and Si (by 1.3% for the “magic mismatch” [9]). Since the previous LEED measurements on Bi(111) indicated that the lateral compression accompanied the vertical expansion of the topmost Bi layer [34], the lateral bond compression in the present study may partly be caused by the interbilayer expansion. We do not observe a clear frequency split for the  $E_g$  mode even at  $n = 3$  BL, partly because of its extremely small amplitude. We actually would not expect the splitting for the  $E_g$  mode, because the interbilayer spacing would not affect the lateral  $E_g$  motions so critically as the vertical  $A_{1g}$  motions.

#### V. CONCLUSION

Phonon dynamics of ultrathin Bi films on Si(111) was investigated as a function of the film thickness close to the structural phase transformation. The coherent  $A_{1g}$  and  $E_g$  phonons of the rhombohedral crystal were clearly observed for Bi films for thicknesses down to 3 BL, below which no phonon mode was detected, in agreement with the structural identifications by LEED. The  $A_{1g}$  phonon redshifted significantly and split into two frequencies at 3 BL, which were attributed to the vertical motion of Bi atoms localized at the surface and subsurface bilayers. By contrast, the  $E_g$  frequency blueshifted with respect to that of the bulk, possibly due to the compressive stress arising from the Bi/Si lattice mismatch. Our results demonstrated the advantage of coherent phonon spectroscopy in the time domain, with extraordinarily high sensitivity to the atomically thin Bi films and high frequency-resolution for the low-frequency oscillations.

#### ACKNOWLEDGMENT

This research was partly supported by JSPS KAKENHI Grant No. 20671002.

- 
- [1] C. R. Ast and H. Höchst, *Phys. Rev. Lett.* **87**, 177602 (2001).
  - [2] P. Hofmann, J. E. Gayone, G. Bihlmayer, Y. M. Koroteev, and E. V. Chulkov, *Phys. Rev. B* **71**, 195413 (2005).
  - [3] T. Hirahara, T. Nagao, I. Matsuda, G. Bihlmayer, E. V. Chulkov, Y. M. Koroteev, P. M. Echenique, M. Saito, and S. Hasegawa, *Phys. Rev. Lett.* **97**, 146803 (2006).
  - [4] T. Hirahara, T. Nagao, I. Matsuda, G. Bihlmayer, E. V. Chulkov, Y. M. Koroteev, and S. Hasegawa, *Phys. Rev. B* **75**, 035422 (2007); T. Hirahara, K. Miyamoto, A. Kimura, Y. Niinuma, G. Bihlmayer, E. V. Chulkov, T. Nagao, I. Matsuda, S. Qiao, K. Shimada, H. Namatame, M. Taniguchi, and S. Hasegawa, *New J. Phys.* **10**, 083038 (2008).
  - [5] S. Murakami, *Phys. Rev. Lett.* **97**, 236805 (2006).
  - [6] Y. M. Koroteev, G. Bihlmayer, E. V. Chulkov, and S. Blügel, *Phys. Rev. B* **77**, 045428 (2008).
  - [7] Z. Liu, C.-X. Liu, Y.-S. Wu, W.-H. Duan, F. Liu, and J. Wu, *Phys. Rev. Lett.* **107**, 136805 (2011).
  - [8] M. Wada, S. Murakami, F. Freimuth, and G. Bihlmayer, *Phys. Rev. B* **83**, 121310 (2011).
  - [9] T. Nagao, J. T. Sadowski, M. Saito, S. Yaginuma, Y. Fujikawa, T. Kogure, T. Ohno, Y. Hasegawa, S. Hasegawa, and T. Sakurai, *Phys. Rev. Lett.* **93**, 105501 (2004).
  - [10] S. Yaginuma, K. Nagaoka, T. Nagao, G. Bihlmayer, Y. M. Koroteev, E. V. Chulkov, and T. Nakayama, *J. Phys. Soc. Jpn.* **77**, 014701 (2008).
  - [11] H. Mönig, J. Sun, Y. M. Koroteev, G. Bihlmayer, J. Wells, E. V. Chulkov, K. Pohl, and P. Hofmann, *Phys. Rev. B* **72**, 085410 (2005).
  - [12] M. Mayrhofer-Reinhartshuber, A. Tamtögl, P. Kraus, K. Rieder, and W. Ernst, *J. Phys.: Condens. Matter* **24**, 104008 (2012).

- [13] A. Tamtögl, P. Kraus, M. Mayrhofer-Reinhartshuber, D. Campi, M. Bernasconi, G. Benedek, and W. E. Ernst, *Phys. Rev. B* **87**, 035410 (2013).
- [14] J. E. Gayone, S. V. Hoffmann, Z. Li, and P. Hofmann, *Phys. Rev. Lett.* **91**, 127601 (2003); J. Gayone, C. Kirkegaard, J. Wells, S. Hoffmann, Z. Li, and P. Hofmann, *Appl. Phys. A* **80**, 943 (2005).
- [15] E. Papalazarou, J. Faure, J. Mauchain, M. Marsi, A. Taleb-Ibrahimi, I. Reshetnyak, A. van Rookeghem, I. Timrov, N. Vast, B. Arnaud, and L. Perfetti, *Phys. Rev. Lett.* **108**, 256808 (2012).
- [16] J. Faure, J. Mauchain, E. Papalazarou, M. Marsi, D. Boschetto, I. Timrov, N. Vast, Y. Ohtsubo, B. Arnaud, and L. Perfetti, *Phys. Rev. B* **88**, 075120 (2013).
- [17] P. Kraus, A. Tamtögl, M. Mayrhofer-Reinhartshuber, G. Benedek, and W. E. Ernst, *Phys. Rev. B* **87**, 245433 (2013).
- [18] G. Q. Huang and J. Yang, *J. Phys.: Condens. Matter* **25**, 175004 (2013).
- [19] J. Yang, G. Huang, and X. Zhu, *Phys. Status Solidi (b)* **250**, 1937 (2013).
- [20] E. Haro-Poniatowski, M. Jouanne, J. F. Morhange, M. Kanehisa, R. Serna, and C. N. Afonso, *Phys. Rev. B* **60**, 10080 (1999).
- [21] J. Zhang, Z. Peng, A. Soni, Y. Zhao, Y. Xiong, B. Peng, J. Wang, M. Dresselhaus, and Q. Xiong, *Nano Lett.* **11**, 2407 (2011).
- [22] R. Peierls, *More Surprises in Theoretical Physics* (Princeton University Press, Princeton, NJ, 1991).
- [23] T. Cheng, J. Vidal, H. Zeiger, G. Dresselhaus, M. Dresselhaus, and E. Ippen, *Appl. Phys. Lett.* **59**, 1923 (1991).
- [24] K. Ishioka, M. Kitajima, and O. Misochko, *J. Appl. Phys.* **100**, 093501 (2006).
- [25] S. L. Johnson, P. Beaud, E. Mohr-Vorobeva, A. Caviezel, G. Ingold, and C. J. Milne, *Phys. Rev. B* **87**, 054301 (2013).
- [26] T. Nagao, T. Doi, T. Sekiguchi, and S. Hasegawa, *Jpn. J. Appl. Phys.* **39**, 4567 (2000).
- [27] C. Bronner and P. Tegeder, *Phys. Rev. B* **89**, 115105 (2014).
- [28] K. Ishioka, A. K. Basak, and H. Petek, *Phys. Rev. B* **84**, 235202 (2011).
- [29] I. Timrov, T. Kampfrath, J. Faure, N. Vast, C. R. Ast, C. Frischkorn, M. Wolf, P. Gava, and L. Perfetti, *Phys. Rev. B* **85**, 155139 (2012).
- [30] K. Yokota, J. Takeda, C. Dang, G. Han, D. N. McCarthy, T. Nagao, S. Hishita, M. Kitajima, and I. Katayama, *Appl. Phys. Lett.* **100**, 251605 (2012).
- [31] S. Xiao, D. Wei, and X. Jin, *Phys. Rev. Lett.* **109**, 166805 (2012).
- [32] [111] in pseudocubic notation corresponds to [0001] in hexagonal notation and to [001] in rhombohedral notation. We use pseudocubic notation throughout this study, unless otherwise noted.
- [33] J. A. Sobota, S.-L. Yang, D. Leuenberger, A. F. Kemper, J. G. Analytis, I. R. Fisher, P. S. Kirchmann, T. P. Devereaux, and Z.-X. Shen, *Phys. Rev. Lett.* **113**, 157401 (2014).
- [34] S. Yaginuma and T. Nagao, *Phys. Rev. B* **82**, 045422 (2010).